RSC Advances

PAPER

View Article Online
View Journal | View Issue

Cite this: *RSC Adv.*, 2025, **15**, 14463

Synergistic enhancement of charge transfer and catalytic activity in CNT@rGO@Cu_2S composite counter electrodes for high-performance quantum dot-sensitized solar cells†

Huu Phuc Dang, *[a] Le Tran, [bc] Le Huu Bao[bc] and Hanh Ngoc Thi Le[d]

Developing cost-effective high-performance counter electrodes (CEs) is critical for improving the efficiency of quantum dot-sensitized solar cells (QDSSCs). In this study, a CNT@rGO@Cu_2S composite CE was synthesized using a hydrothermal method, incorporating carbon nanotubes (CNTs), reduced graphene oxide (rGO), and Cu_2S nanoparticles to enhance the charge transfer and catalytic activity. Structural characterization (XRD, Raman, FESEM, and HRTEM) confirmed the successful integration of the Cu_2S nanoflowers within the rGO matrix. CNTs formed a conductive network that prevented rGO restacking and facilitated electron transport. Electrochemical analysis (CV, EIS, and Tafel polarization) demonstrated the superior electrocatalytic activity of the 6% CNT@rGO@Cu_2S composite, exhibiting the highest exchange current density (J_0) and lowest charge transfer resistance (R_{ct1}), indicating efficient polysulfide redox reactions. When employed in QDSSCs with a CdS/CdSe co-sensitized photoanode, the 6% CNT@rGO@Cu_2S CE achieved a power conversion efficiency (PCE) of 5.965%, surpassing those of rGO@Cu_2S (5.322%) and conventional Pt-based CEs (1.96%). The superior performance is attributed to the optimized Fermi level alignment with the redox couple, enhanced charge mobility due to the CNTs, and improved electrolyte penetration.

Received 31st March 2025
Accepted 28th April 2025

DOI: 10.1039/d5ra02228b

rsc.li/rsc-advances

1 Introduction

Quantum dot-sensitized solar cells (QDSSCs) have garnered significant attention in the field of renewable energy research because of their high potential for efficiently converting sunlight into electrical energy.[1,2] These solar cells utilize quantum dots and semiconductor nanoparticles that are capable of absorbing light and generating electron–hole pairs. The quantum properties of these dots allow QDSSCs to absorb a wider portion of the solar spectrum, enabling enhanced light absorption and energy conversion efficiency compared with traditional solar cells.[3–7] However, the overall performance of QDSSCs depends on the properties of the quantum dots and the materials used in the counter electrodes. The counter electrode plays a critical role in facilitating redox reactions and must possess high electrical conductivity, catalytic activity, and stability in the operational environment of the cell. Traditionally, platinum (Pt) has been used as the counter electrode material owing to its excellent catalytic properties; however, its high cost and scarcity have prompted researchers to explore alternative materials.[8] Among the most promising alternatives are carbon-based materials (such as carbon,[9–11] graphene oxide (GO), reduced graphene oxide (rGO),[5,12,13] carbon nanotubes (CNTs)),[14] and transition metal sulfides (such as MoS_2, PbS, and Cu_2S)[15–17] which have favorable electrochemical and catalytic properties.

CNTs are exceptional candidates for counter-electrode applications because of their unique electron mobility and conductivity. Compared to other carbon-based materials, such as graphene, CNTs possess a tubular structure that provides one-dimensional electron pathways, allowing electrons to move rapidly through the material.[18,19] This high electron mobility reduces the series resistance of the electrode, which is crucial for improving the power conversion efficiency (PCE) of QDSCs.[20,21] Furthermore, the tubular structure of CNTs offers mechanical strength and flexibility, allowing CNTs to act as scaffolds that support and disperse other active materials. Li *et al.* (2021)[22] explored boron-doped CNTs (B-CNT) as a substitute for Pt in QDSC counter electrodes. The B-CNT-based electrodes exhibited catalytic properties comparable to those of Pt,

[a]*Faculty of Fundamental Science, Industrial University of Ho Chi Minh City, Ho Chi Minh City 700000, Vietnam. E-mail: danghuuphuc@iuh.edu.vn*

[b]*Faculty of Physics & Engineering Physics, VNUHCM-University of Science, Ho Chi Minh City, Vietnam*

[c]*Vietnam National University Ho Chi Minh City, Ho Chi Minh City, Vietnam*

[d]*Faculty of Chemical Engineering, Ho Chi Minh City University of Industry and Trade, 140 Le Trong Tan Street, Tay Thanh Ward, Tan Phu District, Ho Chi Minh City, Vietnam*

† Electronic supplementary information (ESI) available. See DOI: https://doi.org/10.1039/d5ra02228b

while significantly reducing the production costs. The doped CNTs not only provided efficient electron transport pathways but also maintained the structural integrity of the material during redox reactions. The combination of CNTs with other materials, such as transition metal sulfides or graphene derivatives, produces a synergistic effect that enhances both the catalytic activity and electron transport. M. Que *et al.* (2014)[23] investigated using CNT/graphene paper composites as counter electrodes in QDSSCs. The synergy between CNTs and graphene provides a large surface area and enhances the electron transfer capability of the electrode. The CNTs maintained their structural integrity, preventing the graphene sheets from restacking, which maximized the active surface area available for catalytic activity. Similarly, Gopi *et al.* (2017)[24] combined CNTs with cobalt sulfide (CoS) to form a hybrid counter electrode for QDSSCs. The study found that the CNT component helped to create an efficient electron transport network. This prevents the aggregation of CoS, preserving a high surface area, which is essential for catalytic reactions in solar cells. In another study, Peter *et al.* (2021)[25] created a hybrid counter electrode using MWCNT combined with Sb_2S_3. The CNTs acted as efficient electron transport scaffolds, while the Sb_2S_3 nanoparticles provided catalytic activity. The researchers observed that CNTs prevented Sb_2S_3 from aggregating, ensuring a high surface area and a uniform distribution of catalytic sites, which improved the redox reaction efficiency in QDSSCs. M. Seol enhances catalytic performance when combined with graphene and Mo metal compounds (Mo_2N, MoS_2 Mo_2C), CNT improves catalytic activity, helping to increase the electrochemical reaction rate, achieving an efficiency of 5.41% for Mo_2N/carbon nanotube (CNT)–rGO CE. CNT acts as a continuous conductive network, enhancing electron transport, reducing resistance, and improving electrochemical performance. Simultaneously, CNT helps maintain the structure of the material, minimize performance degradation after many operating cycles, and prevent the aggregation of nanoparticles, ensuring the uniform distribution of active materials, thereby optimizing the reaction surface.[26] Gopi *et al.* (2018) investigated the application of three-component MoCuSe and rGO/CNT hybrid counter electrodes in QDSSCs. The study demonstrated that a highly conductive CNT@rGO network developed on electrochemically active MoCuSe particles offered a substantial surface area and facilitated a rapid electron transport rate at the counter electrode/electrolyte interface. The conversion efficiency achieved (8.28%) was nearly double that of the MoCuSe counter electrode alone (4.04%).[27]

In our previous work, we investigated binary Cu_2S@rGO composites as counter electrodes for QDSSCs.[28,29] While these materials exhibit promising catalytic activity, their performance is constrained by the tendency of rGO sheets to restack and aggregate, which reduces the accessible surface area and limits electrolyte diffusion and active site exposure. Additionally, the lack of a well-defined conductive network hinders efficient charge transport. To address these limitations, the present study introduces a ternary CNT@rGO@Cu_2S nanocomposite, where the incorporation of CNTs effectively prevents rGO aggregation by acting as nanoscale spacers and forming a robust 3D conductive framework. This architecture enhances both the electrical conductivity and dispersion of the Cu_2S nanoparticles, resulting in improved interfacial contact and catalytic activity. By systematically tuning the CNT content (4, 6, and 8%), we optimized the balance between conductivity and catalytic site accessibility. Structural and electrochemical correlations were established through comprehensive characterization using XRD, Raman spectroscopy, XPS HRTEM, and EIS.

2 Material and method

Graphene oxide (GO), polyvinylpyrrolidone (PVP) $(C_6H_9NO)_n$, thiourea $SC(NH_2)_2$, ethylene glycol $(CH_2OH)_2$, copper(I) chloride (CuCl), polyethylene glycol (PEG) $(C_6H_9NO)_n$, carbon nanotube (CNTs), selenium (Se), sodium sulfite (Na_2SO_3), sodium hydroxide (NaOH), cadmium acetate dihydrate $(CH_3COO)_2$-$Cd\cdot 2H_2O$, copper(II) chloride ($CuCl_2\cdot 2H_2O$), zinc nitrate hexahydrate ($Zn(NO_3)_2\cdot 6H_2O$), and sodium sulfide nonahydrate ($Na_2S\cdot 9H_2O$) were procured from Sigma-Aldrich. Methanol (CH_3OH), ethanol (C_2H_6O), sulfur (S), acid chloride (HCL), and potassium chloride (KCl) were obtained from Aladdin Reagent Co. Ltd. In addition, titania paste (43T mesh) and fluorine-doped tin oxide (FTO) glass (7 Ω sq^{-1}) were sourced from Dyesol.

2.1 Fabrication of photoanode FTO/TiO_2/CdS/CdSe:Cu/ZnS

The FTO/TiO_2/CdS/CdSe:Cu/ZnS photoanodes were fabricated through a combination of screen printing and the sequential ion layer adsorption and reaction (SILAR) technique. Initially, the FTO glass substrates were ultrasonically cleaned in acetone, ethanol, and deionized water to remove contaminants. A TiO_2 film was then deposited onto the FTO surface using the screen-printing method, followed by drying at 80 °C for 30 min and subsequent annealing at 450 °C for 30 min to enhance the crystallinity. After sintering, CdS and Cu^2-doped CdSe quantum dots (with a Cd^{2+}/Cu^{2+} molar ratio of 0.3) were deposited onto the TiO_2 film *via* the SILAR method. The precursor solutions for Cd, S, and Se were prepared according to a previously reported.[30] A ZnS protective layer was introduced using the SILAR technique, employing 0.1 M $Zn(NO_3)_2$ and 0.1 M Na_2S in ethanol as precursor solutions to improve stability and surface passivation further. Finally, the assembled photoanodes were rinsed with ethanol and stored in an inert gas atmosphere in the dark for further use.

2.2 Fabrication of photocathode FTO/CNT@Cu_2S@rGO

The CNT@rGO@Cu_2S hybrid catalyst was synthesized using a two-step hydrothermal approach.

Step 1: synthesis of Cu_2S nanoparticles.

Cu_2S nanoparticles were synthesized by dissolving 0.1 M (0.398 g) copper(I) chloride (CuCl), 0.1 M (0.304 g) thiourea ($SC(NH_2)_2$), and polyvinylpyrrolidone (PVP) in 20 mL of ethylene glycol (EG), followed by mixing with 40 mL of deionized water under vigorous stirring for 30 minutes. The homogeneous solution was then transferred into a 100 mL autoclave and

heated at 180 °C for 10 h. After natural cooling to room temperature, the precipitate was collected *via* filtration, thoroughly washed with deionized water and ethanol, and dried overnight at 60 °C.

Step 2: preparation of CNT@rGO@Cu_2S composite.

In the second step, CNTs (sourced from Carbon Nano-Material Technology Co., Ltd) and reduced graphene oxide (rGO), prepared as described in ref. 30 were mixed in ethanol (10 mL) with *x*-weight ratios ($x = 4$, 6, and 8) and dispersed *via* ultrasonication. A suspension containing (0.03 g) and Cu_2S (0.1 g) was prepared in 50 mL of deionized water, magnetically stirred for 30 min, and subjected to ultrasonication for 1 h to ensure uniform dispersion. The mixture was transferred into a 100 mL autoclave, sealed, and heated at 180 °C for 10 h. After cooling to room temperature, the resulting product was filtered, rinsed with ethanol and deionized water, and dried at 60 °C overnight.

2.3 Counter electrode fabrication

The synthesized CNT@rGO@Cu_2S composite was blended with 5 mL of ethanol and 0.5 g of polyethylene glycol (PEG) to form a viscous slurry. This slurry was then applied to an FTO substrate *via* screen printing to fabricate a counter electrode (CE) with an active area of 0.25 cm^2. Finally, the electrode was annealed at 350 °C for 30 min to enhance the electrocatalytic properties (Scheme 1).

2.4 Assembly of QDSSCs

The electrodes were assembled with Surlyn packing film and infused with an electrolyte solution containing 2 M Na_2S, 2 M S, and 0.2 M KCl, resulting in a cell with a 1 cm^2 active area.

2.5 Measurements and characterizations

The phase compositions and crystallinities of the nanocomposites were determined using a Bruker D8 Advance X-ray diffractometer. Microstructural analysis, including lattice fringes and diffraction patterns, was performed using high-resolution transmission electron microscopy (HRTEM) and selected-area X-ray diffraction (XRD-SAED) JEM 2100 electron microscope (JEOL, Tokyo, Japan). The surface morphology and elemental composition of the samples were examined using an S-4800 FESEM (Hitachi, Japan) equipped with an energy dispersive X-ray (EDX) detector. Raman spectra were recorded with a Horiba (XploRA PLUS) spectrometer at a 532 nm laser wavelength. XPS was used to characterize the surface chemical composition using a VersaProbe II spectrometer at a pressure of 2×10^{-8} mTorr in a vacuum chamber. Electrochemical impedance spectroscopy (EIS), cyclic voltammetry (CV), and Tafel polarization measurements were performed using a CHI 650E electrochemical workstation (CH Instruments, USA) in a three-electrode configuration, with a platinum wire as the counter electrode and Ag/AgCl as the reference electrode. CV and Tafel measurements were carried out in a three-electrode configuration using a platinum wire as the counter electrode and an Ag/AgCl reference electrode in a polysulfide electrolyte consisting of 0.1 M S, 0.1 M Na_2S, and 0.1 M KCl. Tafel polarization curves were recorded over the potential range of −0.9 V to 0.1 V *vs.* Ag/AgCl at a scan rate of 1 mV s^{-1}. EIS was conducted under dark conditions over a frequency range of 100 kHz to 0.1 Hz with an AC perturbation amplitude of 10 mV. The photovoltaic performance of the QDSSCs was assessed by recording the current density *versus* voltage (*J*–*V*) characteristics using a Keithley 2450 source meter under 300 W m^{-2} standard solar illumination (Xe lamp with AM 1.5 filter).

3 Result and discussion

3.1 XRD

The crystallinity of the Cu_2S decorated rGO sheets and CNT was determined by X-ray diffraction (XRD) (Fig. 1). The rGO powder exhibits a diffraction peak at 25.9°, corresponding to the (002) plane. The peak of CNTs was typically observed around $2\theta = 25.8°$.[31] The XRD patterns of the *x*% CNT/rGO@Cu_2S ($x = 4$, 6, and 8) nanocomposites revealed a broad peak at approximately $2\theta = 24$–26°, indicating restoration of the graphitic structure with the disappearance or significant reduction of GO. *x*% CNT/rGO@Cu_2S nanocomposites show peaks corresponding to Cu_2S crystal structure (chalcocite) (JCPDS, pdf no. 26-1116) at 2θ values of ∼26.7°, ∼29°, ∼37.4°, ∼45.7°, and ∼48.6°, correspond

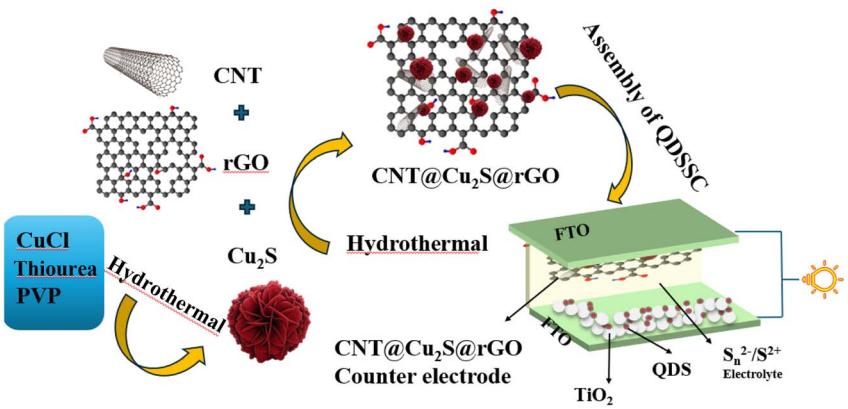

Scheme 1 Synthesis of the FTO/CNT@Cu_2S@rGO counter electrode.

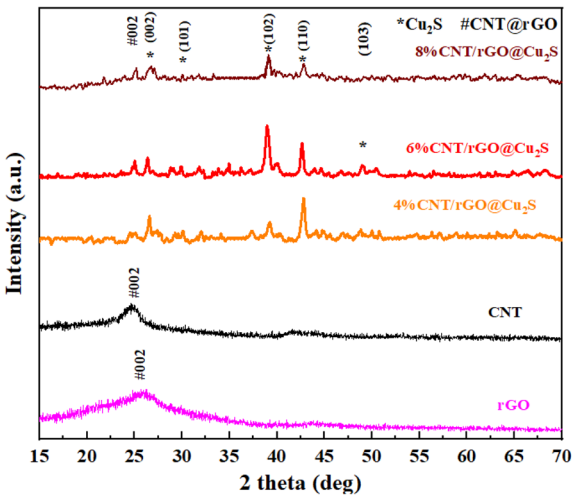

Fig. 1 XRD patterns of rGO, CNT, and *x*% CNT/rGO@Cu_2S ($x = 4, 6, 8$) nanocomposites.

to (002), (101), (102), (110), (103) and (004). The broad peak of rGO at 24–26° may still be visible, but potentially less intense owing to the Cu_2S coating, possibly weak peaks from CNTs, typically around $2\theta = 26°$ (overlapping with rGO).

Raman spectroscopy was employed to analyze the structural features of GO, rGO, and various compositions of the *x*% CNT/rGO@Cu_2S ($x = 4, 6,$ and 8) nanocomposites, revealing material interactions and transformations during processing (Fig. 2). Raman spectroscopy reveals Cu_2S-related peaks at 268 cm^{-1} and 472 cm^{-1}, corresponding to lattice vibrational modes crucial for enhancing charge transfer and catalytic efficiency.[32] The incorporation of CNTs influenced the Raman spectra by altering the D band intensity and shifting the G band position, indicating strong electronic interactions with rGO and Cu_2S. Additionally, CNTs contribute to an increased 2D peak (2766 cm^{-1}) intensity, reflecting better graphitization and improved carrier transport properties, which enhance the overall conductivity and electrocatalytic performance.[33] These peaks indicated the successful incorporation of Cu_2S into the composite structure, facilitating polysulfide redox reactions. Additionally, the D (~1342 cm^{-1}) and G (~1576 cm^{-1}) bands confirm rGO formation, with the degree of disorder and sp^2 hybridization influencing electron mobility and catalytic performance.[34,35] The I_D/I_G ratio, indicative of the defect density, was lowest in the 6% CNT@rGO@Cu_2S sample, suggesting enhanced conductivity due to reduced disorder.[36] The lower defect density facilitates improved electron mobility by reducing charge scattering and recombination losses, enhancing the efficiency of charge transport within the counter electrode. Additionally, the well-ordered carbon structure promoted faster redox reaction kinetics at the CE/electrolyte interface, contributing to superior electrocatalytic performance.

FTIR spectroscopy was employed to complement the Raman and XRD analyses by identifying the functional groups in the composite materials (Fig. 3). The FTIR spectrum of GO exhibits characteristic peaks at 1722 cm^{-1} (C═O), 1620 cm^{-1} (C═C), 1225 cm^{-1} (C–O–C), 1050 cm^{-1} (C–O) and a broad peak at 3200–3500 cm^{-1} (O–H stretching),[37] indicating the presence of oxygen functionalities. Upon reduction to rGO, the intensity of these oxygen-related peaks decreased significantly, confirming the successful removal of oxygen groups and restoration of the sp^2 carbon network.[38] For the CNT@rGO@Cu_2S composites, FTIR analysis revealed a reduction in oxygen functional groups, which is consistent with the XRD findings that indicate the reestablishment of graphitic structures. Additionally, the Cu–S stretching vibration at ~611 cm^{-1} confirms the presence of Cu_2S.[32] The integration of CNTs within the composite further

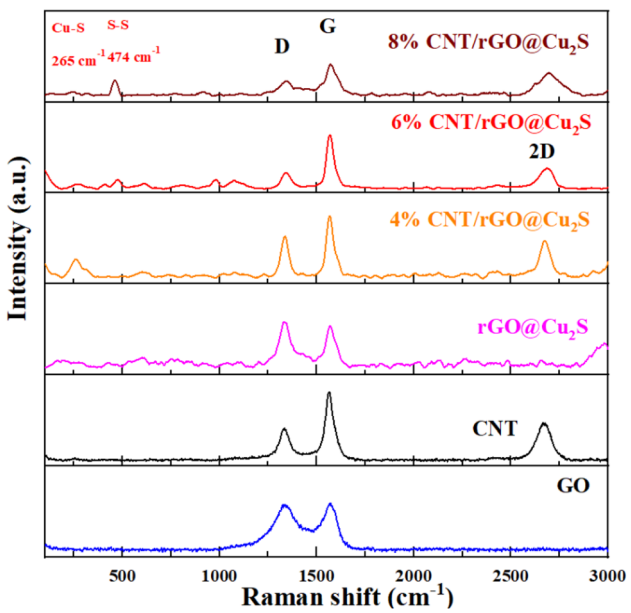

Fig. 2 Raman spectrum of GO, CNT, rGO@Cu_2S, and *x*% CNT/rGO@Cu_2S ($x = 4, 6, 8$) nanocomposites.

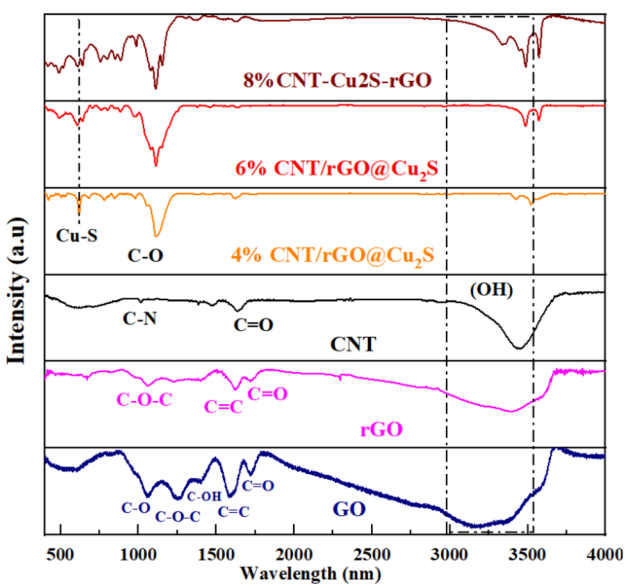

Fig. 3 FT-IR of GO, rGO, CNT and *x*% CNT/rGO@Cu_2S ($x = 4, 6, 8$) nanocomposites.

enhanced the graphitic structure, as evidenced by the intensified C=C peak (~1625 cm^{-1}), supporting the improved electronic conductivity observed in the electrochemical measurements.[39]

FESEM analysis provides a comprehensive understanding of the morphological structure and spatial distribution of the Cu_2S nanoparticles, CNTs, and rGO within the nanocomposites, as shown in Fig. 4. The micrographs revealed that the Cu_2S nanoparticles exhibited spherical to nanoflower-like structures, with sizes ranging from 50 to 200 nm, and were uniformly anchored onto rGO sheets (Fig. 4b). The rGO nanosheets (Fig. 4a), with lateral dimensions extending to several micrometers, displayed a wrinkled and layered morphology, preventing excessive aggregation of Cu_2S while maintaining a high surface area. CNTs, with diameters of 10–30 nm and lengths extending to several micrometers, form a three-dimensional conductive network interwoven with rGO, effectively preventing rGO restacking and enhancing charge transport pathways. The variation in CNT content (4%, 6%, and 8%) significantly influenced the porosity, conductivity, and catalytic activity of the composite. The 6% CNT@rGO@Cu_2S composite (Fig. 4d) exhibited an optimal porous architecture, ensuring efficient electrolyte diffusion, maximum catalytic site exposure, and enhanced charge transfer. In contrast, the 8% CNT composite (Fig. 4e) showed aggregation of CNTs, which blocked the active sites and hindered electrolyte penetration, thus reducing electrocatalytic efficiency. The 4% CNT composite (Fig. 4c), which is more dispersed, lacks sufficient interconnectivity between CNTs and rGO, leading to a higher charge transfer resistance (R_{ct}) and lower catalytic activity. These morphological characteristics directly correlated with the electrochemical performance, where the 6% CNT@rGO@Cu_2S composite achieved the best balance between structural integrity, electrical conductivity, and catalytic efficiency. This detailed structural analysis highlights the importance of the CNT content in optimizing the counter electrode performance of QDSSCs, demonstrating that a well-structured, interconnected network is essential for enhancing the charge mobility and redox reaction kinetics at the CE/electrolyte interface.

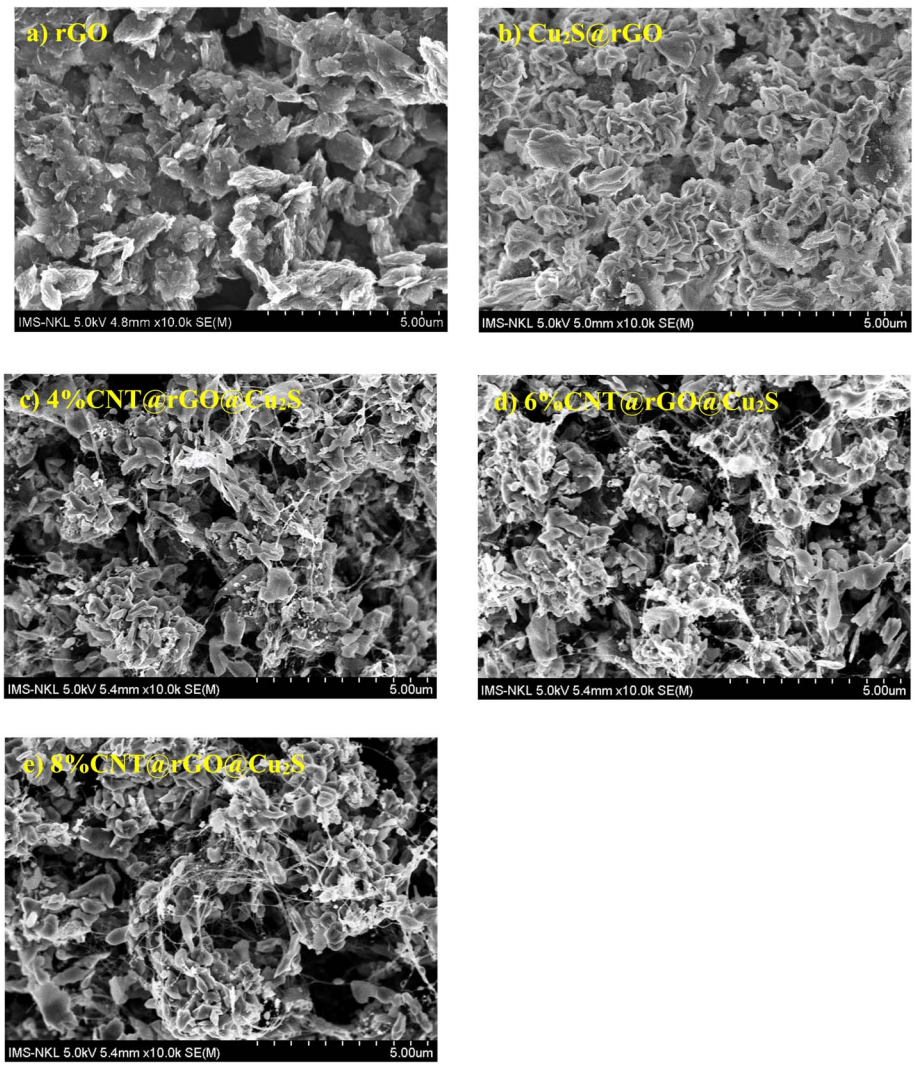

Fig. 4 FESEM images of (a) rGO, (b) rGO@Cu_2S, (c) 4% CNT/rGO@Cu_2S, (d) 6% CNT/rGO@Cu_2S, and (e) 8% CNT/rGO@Cu_2S nanocomposites.

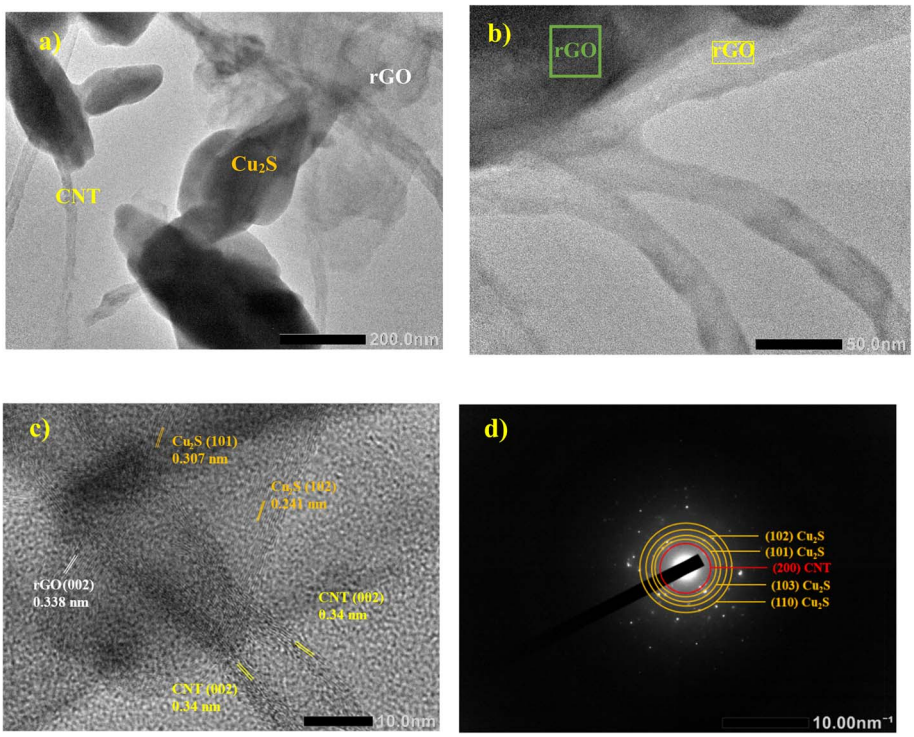

Fig. 5 (a and b) TEM and (c) HRTEM images and (d) SEAD pattern of 6% CNT/rGO@Cu_2S nanocomposites.

Fig. 5a and b present TEM images of the CNT@rGO@Cu_2S nanocomposite, revealing Cu_2S nanoflower-like crystalline particles uniformly embedded within wrinkled rGO sheets and interwoven with CNTs, forming a conductive network. The nanoflower morphology of Cu_2S, with an estimated size of 50–200 nm, provides an expanded catalytic surface area, which is crucial for enhancing electrochemical performance. The TEM images also indicate that CNTs were well dispersed throughout the rGO matrix, preventing restacking of the rGO sheets and facilitating better charge transport pathways. Fig. 5c and d further confirm these structural characteristics through high-resolution TEM (HRTEM) imaging, where distinct lattice fringes are observed: a *d*-spacing of 0.35 nm, corresponding to the (002) plane of rGO, indicating well-ordered graphitic stacking. The *d*-spacing of 0.352 nm was associated with the (111) plane of Cu_2S, confirming the crystalline nature of the embedded Cu_2S nanostructures. The HRTEM images highlight the successful integration of Cu_2S within the rGO–CNT framework, demonstrating a synergistic interaction between the components. The selected area electron diffraction (SAED) pattern provided valuable insights into the crystallinity and phase composition of the CNT@rGO@Cu_2S composite. The presence of distinct diffraction rings corresponding to the (101), (102), (103), and (110) planes of Cu_2S confirms the successful formation of crystalline CuS nanoparticles. Additionally, the (200) diffraction ring associated with CNTs highlights their well-ordered graphitic structure, indicating their role in enhancing electrical conductivity. While rGO also exhibits a characteristic (002) diffraction ring around 0.34–0.35 nm, it may overlap with CNT.

Energy dispersive X-ray (EDX) mapping and spectrum analysis are powerful techniques used to characterize the elemental composition and distribution of the nanocomposites, as shown in Fig. 6. For the 6% CNT/rGO@Cu_2S nanocomposite (Fig. 6e–h), EDX mapping provides a visual representation of the carbon (C), copper (Cu), and sulfur (S) distributions across the sample. Carbon showed a uniform distribution, representing both CNTs and rGO. Copper and sulfur appeared colocalized, indicating the presence of Cu_2S. In addition, areas with higher carbon concentrations may indicate the presence of CNT clusters. The carbon peak intensity is significant because of the presence of CNTs and rGO. Moreover, the ratio of the Cu to S peaks should be approximately 2 : 1, reflecting the Cu_2S stoichiometry. Comparing rGO@Cu_2S (Fig. 6i) and 6% CNT/rGO@Cu_2S (Fig. 6j), the increased carbon atomic percentage in the latter reflects the contribution of CNTs, which improves electron mobility, prevents rGO restacking, and enhances Cu_2S dispersion. This structural optimization results in superior electrochemical and photovoltaic performances, demonstrating the synergistic role of CNTs in enhancing the counter electrode functionality for high-efficiency QDSSCs.

Fig. 7 shows the high-resolution XPS spectra of the 6% CNT/rGO@Cu_2S composite: (a) Cu 2p, (b) S 2p, (c) C 1s, (d) O 1s, and (e) the survey spectrum. In Fig. 7a, the Cu 2p spectrum displays prominent peaks at ~932.4 eV (Cu $2p_3/_2$) and ~952.3 eV (Cu $2p_1/_2$), characteristic of Cu^+ in Cu_2S, with minimal satellite features, indicating negligible Cu^{2+} contamination.[40] Fig. 7b shows the S 2p spectrum with a doublet at ~161.8 eV (S $2p_3/_2$) and ~163.0 eV (S $2p_1/_2$), confirming the presence of S^{2-} species

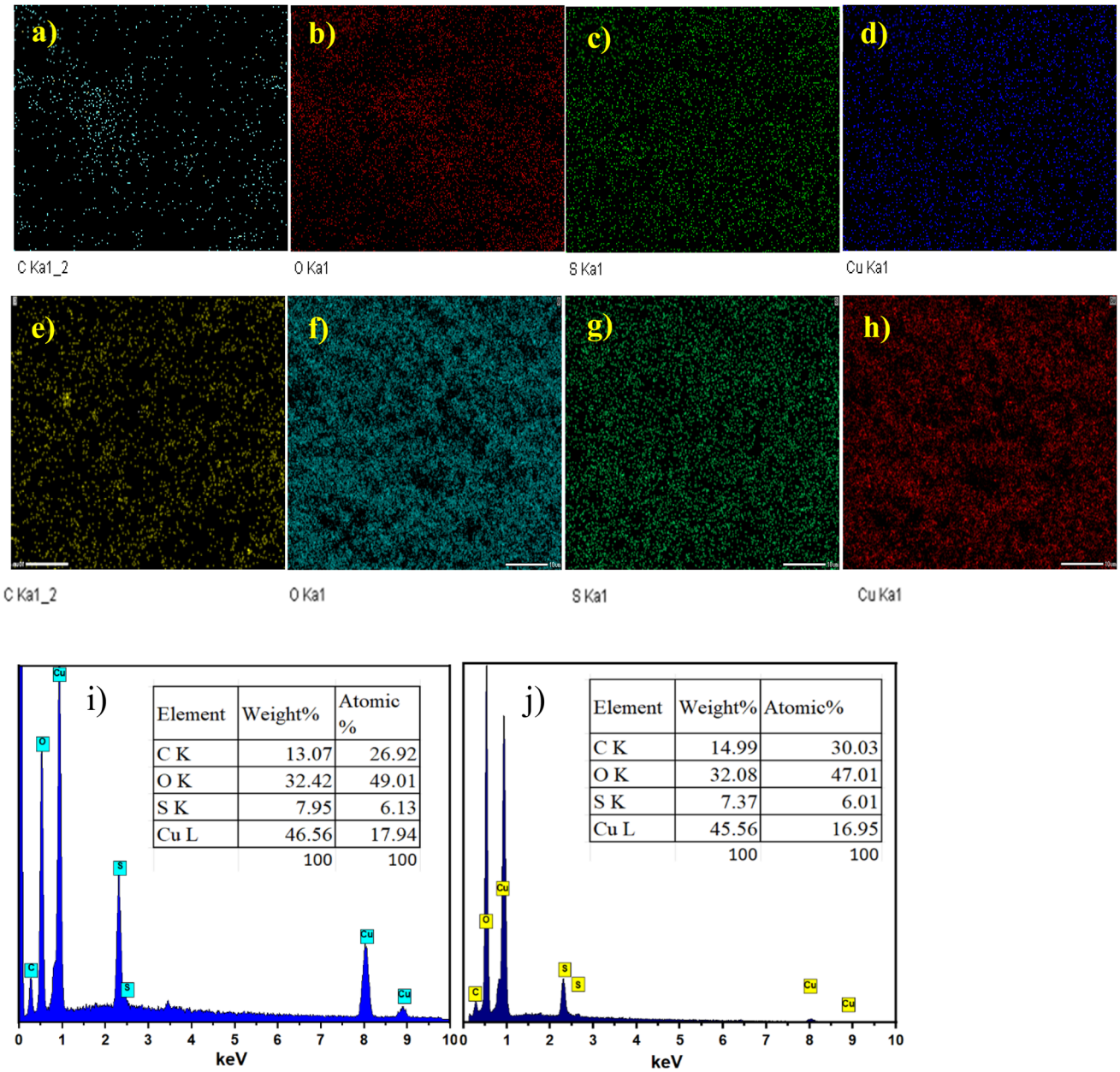

Fig. 6 EDX element mapping image of (a) carbon (C), (b) oxygen (O), (c) sulphur (S), (d) copper (Cu) of rGO@Cu_2S CE, (e) carbon (C), (f) oxygen (O), (g) sulphur (S), (h) copper (Cu) of 6% CNT/rGO@Cu_2S, and atomic percentage of elements (i), of rGO@Cu_2S, and (j) 6% CNT/rGO@Cu_2S.

consistent with copper(I) sulfide.[41] The C 1s spectrum (Fig. 7c) shows a dominant peak at ~284.6 eV, corresponding to sp^2-hybridized carbon (C–C/C=C), which is a clear signature of carbon nanotubes (CNTs) and rGO. Besides, two peaks at ~286.2 eV (C–O) and ~288.4 eV (O–C=O), indicating partial reduction of GO and effective integration of CNTs.[42,43] The deconvoluted O 1s spectrum reveals three primary components centered at ~531.8 eV (C=O), ~532.9 eV (C–O), and ~530.1 eV (Cu–O).[44,45] The C=O and C–O peaks arise from the residual oxygenated functional groups on rGO and CNTs (Fig. 7d). The Cu–O component suggests partial surface oxidation of Cu_2S during synthesis or post-treatment exposure or possible interfacial Cu–O–C coordination with oxygen-containing groups in the carbon matrix. This interfacial bonding may enhance nanoparticle anchoring and contribute to the improved charge transfer across the composite interface. The survey spectrum in Fig. 7e confirms the elemental presence of Cu, S, C, and O, thus validating the structural integrity of the composite.

3.2 Electrochemical characterization

Cyclic voltammetry (CV) was performed to assess the electrocatalytic activity of the synthesized counter electrodes (CEs) in facilitating the polysulfide redox reaction S^{2-}/S_n^{2-} in QDSSCs (Fig. 8). The electrochemical measurements were conducted in a three-electrode setup using Pt and Ag/AgCl electrodes, within 0.1 M S, 0.1 M Na_2S, and 0.1 M KCl, at a scan rate of 10 mV s^{-1}.

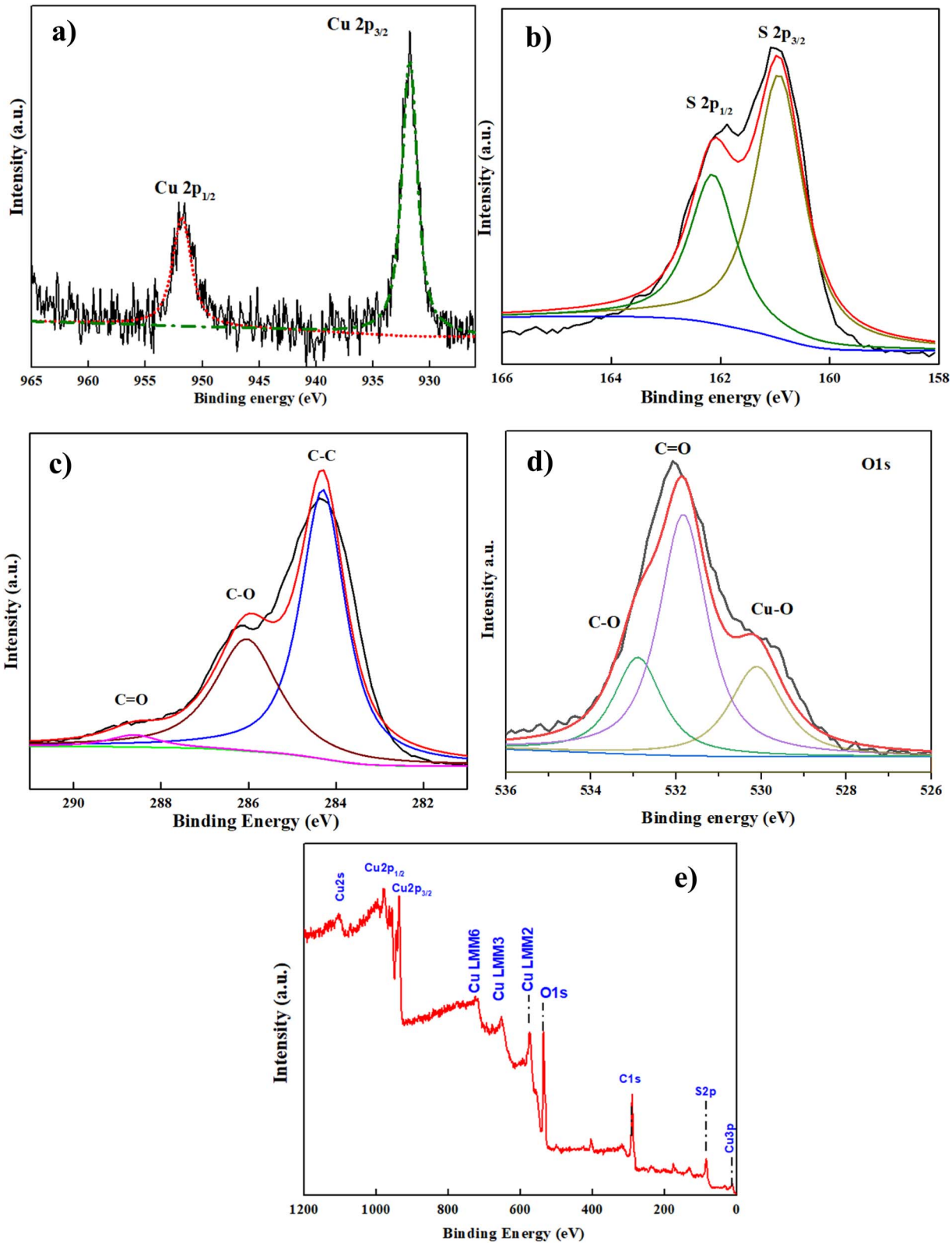

Fig. 7 (a) Cu 2p of (b) S 2p, (c) C 1s, (d) O 1s, and (e) XPS survey spectrum high resolution of 6% CNT/rGO@Cu_2S.

The recorded CV curves displayed two key peaks: (1) an anodic peak corresponding to the oxidation of S_2^- and (2) a cathodic peak associated with the reduction of S_n^{2-} to S^{2-}, confirming the redox activity of the system. As shown in Fig. 8a, the *x*% CNT/rGO@Cu_2S nanocomposite exhibited a significantly higher cathodic current density than the rGO- and Cu_2S-based

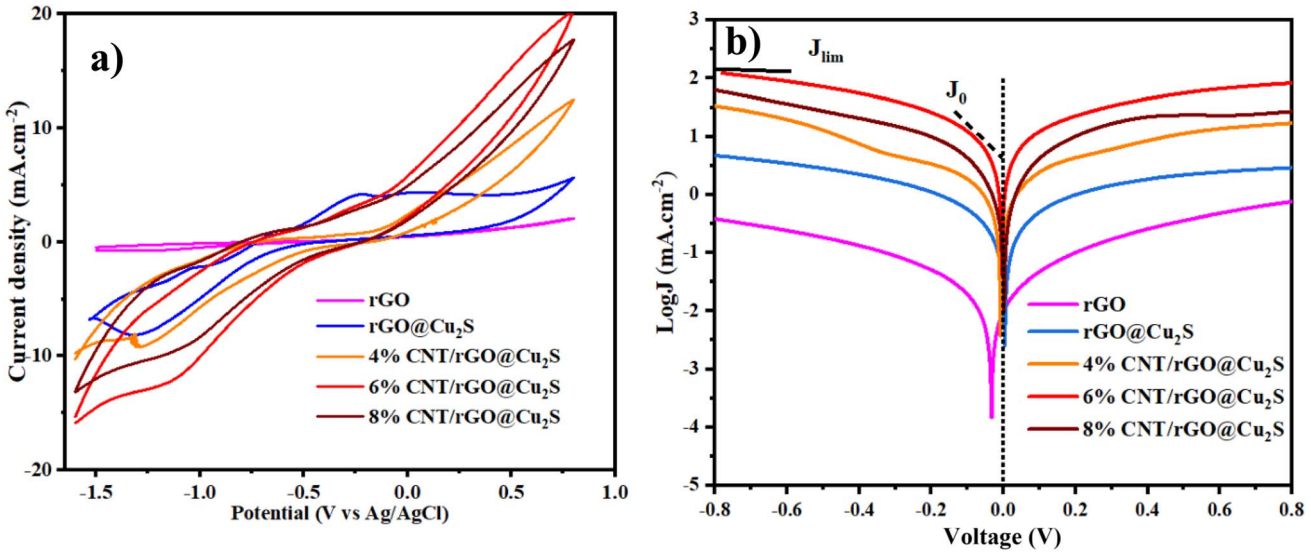

Fig. 8 (a) CV plots measured in 0.1 M S, 0.1 M Na_2S, and 0.1 M KCl using a three-electrode setup at 10 mV s^{-1} scan rate; (b) Tafel polarization of rGO, rGO@Cu_2S and *x*% CNT/rGO@Cu_2S (x = 4, 6, 8) CEs.

electrodes, indicating enhanced electrocatalytic capability for polysulfide reduction. Among the tested compositions, the 6% CNT/rGO@Cu_2S electrode displayed the highest cathodic current density (6.72 mA cm^{-2}), attributed to optimized synergy between CNTs, rGO, and Cu_2S. The superior electrocatalytic performance of this composite was attributed to the integration of CNTs within the rGO matrix, which played a crucial role in establishing a highly conductive 3D framework. This interconnected network prevented rGO restacking, enhanced charge mobility, and ensured improved electrolyte penetration, all of which are essential for efficient catalytic activity. Moreover, the presence of the Cu_2S nanoparticles further enhanced the electrocatalytic efficiency by providing abundant active sites for the polysulfide redox reaction. The synergistic interaction between CNTs, rGO, and Cu_2S not only accelerated the charge transfer kinetics but also improved the structural stability and minimized resistive losses.

Besides, the onset potential for reduction in the CV curves of 6% CNT@rGO@Cu_2S shifted more positively compared to rGO and rGO@Cu_2S, indicating that its Fermi level is better aligned with the redox potential of the S_2^-/Sn^{2-} couple (4.6–4.7 eV *vs.* vacuum).[46,47]

$$E_F = -(E_{onset} + 4.44 + 0.197) \text{ (for vacuum)}$$

This alignment facilitates more efficient electron injection from the counter electrode into the electrolyte, thereby enhancing the charge transfer kinetics and reducing the overpotential losses. The Fermi level of the counter electrode should be close to or slightly above the redox potential of the electrolyte to promote fast electron transfer. The 6% CNT/rGO@Cu_2S electrode has a Fermi level of −4.157 eV, which is closest to the redox potential of the polysulfide couple (−4.6 eV) among all tested CEs (Table 1).

Table 1 Onset potential and Fermi level of rGO, rGO@Cu_2S, and *x*% CNT/rGO@Cu_2S (x = 4, 6, 8) CEs

Counter electrode	Onset potential (V *vs.* Ag/AgCl)	Fermi level (eV *vs.* vacuum)
rGO	−0.23	−4.407
rGO@Cu_2S	−0.30	−4.337
4% CNT/rGO@Cu_2S	−0.37	−4.267
6% CNT/rGO@Cu_2S	−0.48	−4.157
8% CNT/rGO@Cu_2S	−0.42	−4.217

The electrocatalytic properties of the synthesized counter electrodes (CEs) were further examined using Tafel polarization measurements, as shown in Fig. 8b. The Tafel plot was characterized by three distinct regions: (1) the polarization region at low potential, (2) the Tafel region with a steep slope at the intermediate potential, and (3) the diffusion region at a higher potential. The Tafel and diffusion zones are particularly relevant for assessing the electrocatalytic efficiency of the electrodes. The exchange current density (J_0), a key indicator of the catalytic activity, was determined by extrapolating the intersection points of the anodic and cathodic branches in the Tafel plots. Additionally, the limiting current density (J_{lim}), which signifies the mass transport limitations, was obtained from the vertical axis in the diffusion region. Among all the samples, 6% CNT/rGO@Cu_2S exhibited the highest J_0 (0.192 mA cm^{-2}), confirming its rapid charge transfer kinetics. The trend in electrocatalytic performance followed the order 6% CNT/rGO@Cu_2S > 4% CNT/rGO@Cu_2S > 8% CNT/rGO@Cu_2S > rGO@Cu_2S > rGO (Table 2). The enhanced performance of the 6% CNT/rGO@Cu_2S electrode was attributed to its optimized CNT-to-rGO ratio, which facilitated a well-distributed 3D conductive framework that promoted efficient electron transfer. While the 4% CNT composition exhibited slightly lower

Table 2 Comparative current density parameters of rGO, rGO@Cu_2S and *x*% CNT/rGO@Cu_2S (x = 4, 6, 8) CEs

Counter electrode	Cathodic peak current density (CV, mA cm^{-2})	Exchange current density J_0 (Tafel, mA cm^{-2})	Limiting current density J_{lim} (EIS, mA cm^{-2})
rGO	2.56	0.082	3.18
rGO@Cu_2S	4.01	0.129	4.23
4% CNT/rGO@Cu_2S	5.18	0.165	5.27
6% CNT/rGO@Cu_2S	6.72	0.192	6.09
8% CNT/rGO@Cu_2S	5.91	0.143	5.47

catalytic activity, the 8% CNT sample showed a decline owing to possible CNT agglomeration, which could hinder active site accessibility and charge transport.

Moreover, the J_0 value of the CE can be used to demonstrate the charge transfer resistance ($R_{ct\text{-}Tafel}$) at the CE/electrolyte interface, as shown in eqn (1):

$$J_0 = \frac{RT}{nFR_{ct\text{-}Tafel}} \quad (1)$$

where R is the gas constant, n is the number of electrons contributing to charge transfer at the interface, T is the temperature, and F is Faraday's constant.

A higher J_0 corresponded to a lower R_{ct}, indicating a faster electron transfer rate and improved catalytic efficiency. These findings confirm that CNT incorporation plays a crucial role in enhancing electrocatalytic performance, with 6% CNT/rGO@Cu_2S achieving the most effective balance between conductivity, active site exposure, and electrolyte interaction.

The limiting current density (J_{lim}), which reflects the diffusion of ionic species at the counter electrode (CE)/electrolyte interface, is directly related to the diffusion coefficient (D) of S_n^{2-}/S^{2-}, as described by eqn (2):

$$J_{lim} = \frac{2nFCD}{l} \quad (2)$$

where D represents the diffusion coefficient of polysulfides, and the other parameters have conventional meanings. As illustrated in Fig. 9b, the 6% CNT@rGO@Cu_2S CE exhibited a significantly higher J_{lim} (6.09 mA cm^{-2}) than the rGO and rGO@Cu_2S electrodes. This suggests an enhanced ionic diffusion rate at the CE/electrolyte interface, which leads to improved reaction kinetics in the polysulfide electrolyte. The higher J_{lim} value of 6% CNT@rGO@Cu_2S can be attributed to the increased S_n^{2-} concentration, which correlated with the enhanced catalytic activity for polysulfide reduction. This improvement likely results from the synergistic effect of CNTs and Cu_2S, which collectively enhances the charge transfer and electrocatalytic efficiency.

To further evaluate and compare the electrocatalytic activities of the various counter electrodes (CEs), we compiled key current density values obtained from cyclic voltammetry (CV), Tafel polarization, and electrochemical impedance spectroscopy (EIS) (Table 2). The 6% CNT@rGO@Cu_2S electrode exhibited the highest cathodic peak current density (6.72 mA cm^{-2}), the largest exchange current density J_0 (0.192 mA cm^{-2}), and the greatest limiting current density J_{lim} (6.09 mA cm^{-2}), confirming its superior charge transfer and catalytic efficiency. These results directly correlate with the structural advantages observed in FESEM, XRD, and Raman analyses, where 6% CNT

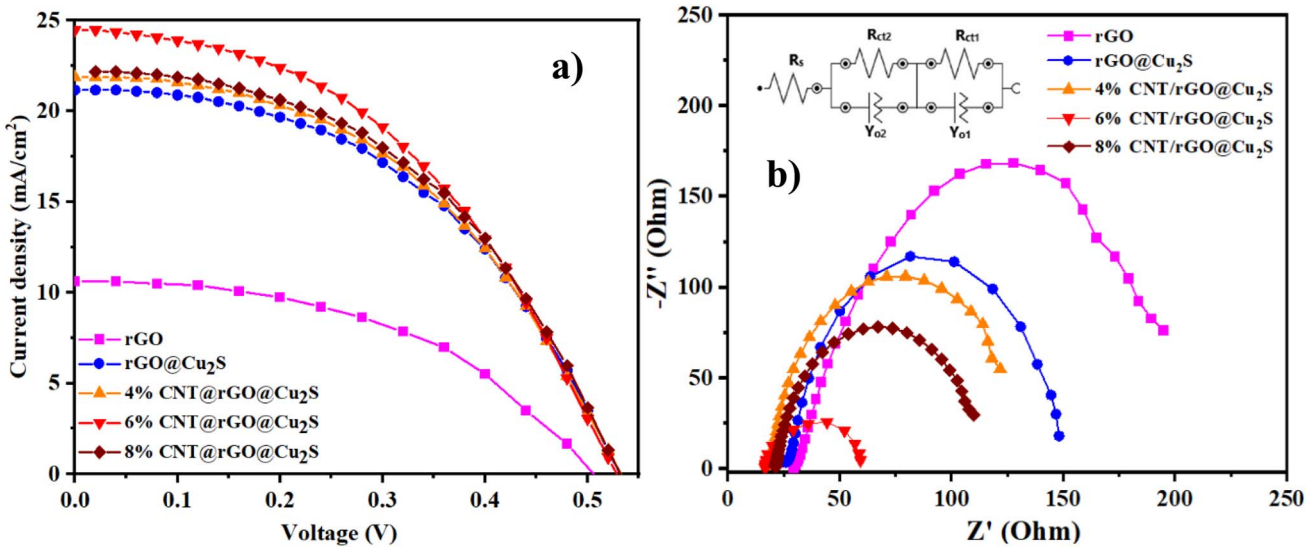

Fig. 9 (a) *J*–*V* curves, (b) Nyquist plots of QDSSCs based on rGO, rGO@Cu_2S, and *x*% CNT/rGO@Cu_2S (x = 4, 6, 8) CEs measured with polysulfide electrolyte (0.1 M S, 0.1 M Na_2S, and 0.1 M KCl), fitted equivalent circuit model shown inset.

Table 3 Photovoltaic and electrochemical performance parameters of QDSSCs based on rGO, rGO@Cu_2S, and *x*% CNT/rGO@Cu_2S ($x = 4$, 6, and 8) CEs. Each value represents the meaning of the three independently fabricated devices

CEs	V_{oc} (V)	J_{sc} (mA cm^{-2})	FF	R_{ct1} (Ω)	PCE (%)
rGO	0.480 ± 0.046	10.622 ± 0.1	0.492 ± 0.004	235.6 ± 2.4	2.511 ± 0.07
rGO@Cu_2S	0.540 ± 0.052	21.157 ± 0.2	0.484 ± 0.004	36.90 ± 0.35	5.322 ± 0.14
4% CNT@rGO@Cu_2S	0.540 ± 0.054	21.872 ± 0.2	0.475 ± 0.004	30.20 ± 0.30	5.408 ± 0.12
6% CNT@rGO@Cu_2S	0.540 ± 0.056	23.299 ± 0.3	0.464 ± 0.004	24.05 ± 0.24	5.965 ± 0.11
8% CNT@rGO@Cu_2S	0.540 ± 0.054	22.165 ± 0.2	0.484 ± 0.004	28.62 ± 0.28	5.575 ± 0.12

loading enabled optimal dispersion, minimal agglomeration, and maximized exposure of electroactive sites. The increasing trend in current density with CNT incorporation up to 6% clearly demonstrates the critical role of CNTs in enhancing electron transport pathways and facilitating redox reaction kinetics, whereas the slight decline at 8% CNT may be attributed to CNT aggregation, which reduces electrolyte accessibility and catalytic surface area.

3.3 Photovoltaic performance of QDSSCs

The photovoltaic performance of the QDSSCs employing different counter electrodes (CEs) was evaluated under AM 1.5G simulated solar illumination (100 mW cm^{-2}), with the corresponding *J–V* characteristics presented in Fig. 9a and the key photovoltaic parameters summarized in Table 3. The 6% CNT@rGO@Cu_2S-based QDSSCs exhibited the highest power conversion efficiency (PCE) of 5.96%, outperforming 8% CNT@rGO@Cu_2S (5.57%), 4% CNT@rGO@Cu_2S (5.41%), rGO@Cu_2S (5.32%), and pure rGO (2.51%). These results highlight the critical role of CNT incorporation in enhancing the charge transport and catalytic activity. The increase in short-circuit current density (J_{sc}) for 6% CNT@rGO@Cu_2S is attributed to the formation of a well-interconnected conductive network, which minimizes charge recombination losses and facilitates rapid electron transport. Additionally, CNTs prevented rGO restacking, improved electrolyte diffusion, and maximized the exposure of active Cu_2S catalytic sites. The open-circuit voltage (V_{oc}) remained relatively stable across all samples, with slight variations due to differences in the charge recombination rates and Fermi level alignment at the CE/electrolyte interface. The superior J_{sc} and PCE observed for 6% CNT@rGO@Cu_2S are supported by electrochemical analyses, where cyclic voltammetry (CV) confirms higher cathodic peak current density, electrochemical impedance spectroscopy (EIS) reveals lower charge transfer resistance (R_{ct1}), and Tafel polarization analysis indicates increased exchange current density (J_0), all of which contribute to enhanced redox reaction kinetics.

The electrochemical impedance spectroscopy (EIS) results presented in Fig. 9b display Nyquist plots of QDSSCs employing various counter electrodes, modeled using an equivalent circuit consisting of a series resistance, two charge-transfer resistances, and the charge transfer resistance (R_{ct1}) at the counter electrode (CE) of QDSSCs using different composite electrodes, R_{ct2} at the photoanode/electrolyte interface, and constant-phase elements (CPEs) representing the interfacial capacitance. Among these, this study focus is on (R_{ct1}), which governs the electron transfer kinetics at the counter electrode—directly reflecting the catalytic efficiency of the CNT@rGO@Cu_2S composites The Nyquist plots exhibit a decreasing semicircle diameter with the incorporation of Cu_2S and CNTs into the rGO matrix, indicating enhanced charge-transfer kinetics at the electrode/electrolyte interface. The pristine rGO sample exhibited the highest R_{ct1} value, suggesting poor catalytic activity and interfacial conductivity. The introduction of Cu_2S significantly reduced R_{ct1}, which is attributed to the improved electrocatalytic activity and electron mobility of Cu_2S. The addition of CNTs further enhances the conductivity by facilitating electron transport pathways, as evidenced by the reduced semicircle diameter, with the 6% CNT/rGO@Cu_2S composition exhibiting the lowest resistance, signifying optimal synergy.

A comparative analysis of various CNT- and rGO-based counter electrodes (CEs) in QDSSCs revealed key trends in

Table 4 Comparison of CNT- and rGO-based counter electrodes in QDSSCs

Counter electrode (CE)	Synthesis method	Sensitizer(s)	J_{sc} (mA cm^{-2})	V_{oc} (V)	FF	PCE (%)	Ref.
CNT@rGO@Cu_2S (6% CNT)	Hydrothermal synthesis	CdS/CdSe	23.299	0.540	0.464	5.965	This work
CNT@rGO@MoCuSe	Two-step hydrothermal	CdS/CdSe	20.540	0.633	0.636	8.280	48
S-doped rGO@CNT	Hydrothermal doping	CdS/CdSe/ZnS	19.290	0.630	0.470	5.700	44
CNT@NiS	Solution deposition	CdS/CdSe	17.530	0.595	0.595	6.410	49
CNT@CoS	Solution deposition	CdS/CdSe	16.140	0.588	0.578	5.780	49
CNT@CuS	Solution deposition	CdS/CdSe	14.500	0.581	0.581	5.050	49
CNT@PbS	Solution deposition	CdS/CdSe	12.500	0.578	0.578	4.270	49
N,S doped rGO@CNT	Doctor blade	CdS/ZnS/N,S:rGO/CNT	12.11	0.609	0.548	4.040	45
N-MC:CNT	Sonicate + screen printing	ZnCuInSSe/ZnS	27.820	0.828	0.720	16.680	50
B doped CNT	Hydrothermal	CdS/CdSe	17.400	0.52	0.520	4.550	22
Pt CE (reference for QDSSCs)	Standard deposition	CdS/CdSe	10.430	0.595	0.316	1.960	48

power conversion efficiency (PCE), charge transport properties, and catalytic activity (Table 4). The integration of CNTs with rGO and metal sulfides offers a promising approach for developing high-performance CEs for QDSSCs. The synergistic effects of these materials lead to enhanced charge mobility, catalytic activity, and electrolyte interaction, ultimately improving photovoltaic performance.

4 Conclusions

This study successfully developed a CNT@rGO@Cu_2S composite counter electrode (CE) for QDSSCs, demonstrating superior electrocatalytic performance, enhanced charge transport, and improved photovoltaic efficiency compared with conventional CEs. Comprehensive structural and spectroscopic analyses (Raman, FTIR, FESEM, and HRTEM) confirmed the successful integration of CNTs, rGO, and Cu_2S into the well-engineered nanocomposite. Raman spectroscopy revealed a reduced I_D/I_G ratio in the 6% CNT@rGO@Cu_2S composite, indicating improved graphitization and enhanced charge transport properties. FTIR analysis verified strong interfacial bonding within the composite, contributing to structural stability and efficient electron mobility. FESEM imaging showed that CNTs formed an interconnected network that prevented rGO restacking, while Cu_2S nanoparticles were uniformly dispersed, providing increased electrochemically active sites. HRTEM analysis confirmed the crystallinity of Cu_2S and rGO, highlighting well-defined lattice fringes that enhanced the charge transfer at the CE/electrolyte interface. Electrochemical characterization (CV, Tafel, and EIS) demonstrated significant improvements in charge-transfer kinetics and catalytic activity. The 6% CNT@rGO@Cu_2S composite exhibited the highest cathodic peak current density in CV, the highest exchange current density (J_0) in Tafel analysis, and the lowest charge transfer resistance (R_{ct1}) in EIS, confirming its superior electrocatalytic properties. These enhancements translated into an impressive power conversion efficiency (PCE) of 5.965% in QDSSCs, outperforming rGO@Cu_2S (5.322%) and Pt-based CEs (1.960%).

Data availability

Data for this article, including origin data, are available at **https://doi.org/10.6084/m9.figshare.28694681**.

Conflicts of interest

The authors declare that they have no competing financial interests or personal relationships that could influence the work reported in this study.

Acknowledgements

This work was supported by the Industrial University of Ho Chi Minh City (IUH), Ho Chi Minh, Vietnam, under grant number 23.1CB03.

References

1 A. J. Nozik, Quantum dot solar cells, *Phys. E*, 2002, **14**, 115–120, DOI: **10.1016/S1386-9477(02)00374-0**.
2 M. Halim, Harnessing Sun's Energy with Quantum Dots Based Next Generation Solar Cell, *Nanomaterials*, 2012, **3**, 22–47, DOI: **10.3390/nano3010022**.
3 M. Eryiğit, S. Mobtakeri, E. P. Gür, E. Temur, T. Ö. Özer, Ü. Demir and E. Gür, Efficient CdS quantum dot sensitized solar cells based on electrochemically reduced graphene oxide (ERGO)/ZnO nanowall photoanodes and MoS2, WS2, CuS cascaded counter electrodes, *Sol. Energy*, 2022, **234**, 348–359, DOI: **10.1016/j.solener.2022.01.030**.
4 E. P. Gür, M. Eryiğit and Ü. Demir, High-performance PbS/CdS quantum dot Co-sensitized hierarchical ZnO nanowall photoanodes decorated on electrochemically reduced graphene, *Electrochim. Acta*, 2023, **438**, 141584, DOI: **10.1016/j.electacta.2022.141584**.
5 E. Praveen, I. J. Peter and S. Murugan, Bi2Ti2O7/PbCdS2/PbS solar cells with NiS@rGO Electrocatalyst: a strategy for enhancing light absorption and polysulfide reduction, *Inorg. Chem. Commun.*, 2023, **158**(2), 111595, DOI: **10.1016/j.inoche.2023.111595**.
6 Y. Zhu, W. Kong, S. Zhu, S. Wang, C. Lei, J. Xu and R. Zhou, In situ Seeded Growth of High-Quality PbS/CdS Quantum Dots for Highly Efficient Photovoltaics, *IEEE J. Photovoltaics*, 2018, **8**, 849–855, DOI: **10.1109/JPHOTOV.2018.2810809**.
7 J. Kusuma, H. R. Chandan and R. G. Balakrishna, Conjugated molecular bridges: a new direction to escalate linker assisted QDSSC performance, *Sol. Energy*, 2019, **194**, 74–78, DOI: **10.1016/j.solener.2019.10.024**.
8 S. Kumar, I. C. Maurya, O. Prakash, P. Srivastava, S. Das and P. Maiti, Functionalized Thermoplastic Polyurethane as Hole Conductor for Quantum Dot-Sensitized Solar Cell, *ACS Appl. Energy Mater.*, 2018, **1**, 4641–4650, DOI: **10.1021/acsaem.8b00783**.
9 Z. Du, Z. Pan, F. Fabregat-Santiago, K. Zhao, D. Long, H. Zhang, Y. Zhao, X. Zhong, J. S. Yu and J. Bisquert, Carbon Counter-Electrode-Based Quantum-Dot-Sensitized Solar Cells with Certified Efficiency Exceeding 11%, *J. Phys. Chem. Lett.*, 2016, **7**, 3103–3111, DOI: **10.1021/acs.jpclett.6b01356**.
10 W. Guo, C. Chen, M. Ye, M. Lv and C. Lin, Carbon fiber/Co9S8 nanotube arrays hybrid structures for flexible quantum dot-sensitized solar cells, *Nanoscale*, 2014, **6**, 3656–3663, DOI: **10.1039/c3nr06295c**.
11 Z. Ali, M. H. Sayyad, A. Ali, M. ur Rahman, N. Anwar and S. Khan, Study on the photovoltaic characteristics of solar cells based on PbS quantum dots and carbon counter electrode, *Mater. Sci. Eng., B*, 2024, **301**, 117144, DOI: **10.1016/j.mseb.2023.117144**.
12 W. Li, S. Zhang, Q. Chen and Q. Zhong, Highly-dispersed CoS2/N-doped carbon nanoparticles anchored on RGO skeleton as a hierarchical composite counter electrode for quantum dot sensitized solar cells, *Chem. Eng. J.*, 2022, **430**, 132732, DOI: **10.1016/j.cej.2021.132732**.

13 S. Monika, M. Mahalakshmi, N. Subha, M. S. Pandian and P. Ramasamy, Graphene quantum dots and CuS microflowers anchored rGO composite counter electrode for the enhanced performance of quantum dot sensitized solar cells, *Diamond Relat. Mater.*, 2022, **125**, 109033, DOI: 10.1016/j.diamond.2022.109033.

14 Y. Wang, W. Liang, D. Hao, M. Li, H. Chen, Y. Gu and S. Wang, Flexible, Stable, and Efficient Counter Electrode for Quantum-Dot-Sensitized Solar Cells Based on Carbon Nanotube Films, *ACS Appl. Mater. Interfaces*, 2024, **16**, 35474–35483, DOI: 10.1021/acsami.4c06961.

15 I. R. Jo, J. A. Rajesh, Y. H. Lee, J. H. Park and K. S. Ahn, Enhanced electrocatalytic activity and electrochemical stability of Cu2S/PbS counter electrode for quantum-dot-sensitized solar cells, *Appl. Surf. Sci.*, 2020, **525**, 146643, DOI: 10.1016/j.apsusc.2020.146643.

16 U. Mehmood and A. Ul Haq Khan, Spray coated PbS nanocrystals as an effective counter-electrode material for platinum free Dye-Sensitized Solar Cells (DSSCs), *Sol. Energy*, 2019, **193**, 1–5, DOI: 10.1016/j.solener.2019.09.035.

17 Z. Tian, Q. Chen and Q. Zhong, Honeycomb spherical 1T-MoS2 as efficient counter electrodes for quantum dot sensitized solar cells, *Chem. Eng. J.*, 2020, **396**, 125374, DOI: 10.1016/j.cej.2020.125374.

18 G. Zhou, C. Cen, S. Wang, M. Deng and O. V. Prezhdo, Electron–Phonon Scattering Is Much Weaker in Carbon Nanotubes than in Graphene Nanoribbons, *J. Phys. Chem. Lett.*, 2019, **10**, 7179–7187, DOI: 10.1021/acs.jpclett.9b02874.

19 Y. Zhu, C. Chen, S. Wu, R. Cheng, L. Cheng and W.-L. Zhou, Edge-dependent ballistic transport through copper-decorated carbon-nanotube–graphene covalent junction with low Schottky barrier, *J. Appl. Phys.*, 2020, **128**, 064302, DOI: 10.1063/5.0009406.

20 A. E.-M. A. Mohamed and M. A. Mohamed, Carbon nanotubes: synthesis, characterization, and applications, in *Carbon Nanomaterials for Agri-Food and Environmental Applications*, Elsevier, 2020, pp. 21–32, DOI: 10.1016/B978-0-12-819786-8.00002-5.

21 H. Habib, M. Alam, M. Aggarwal, I. S. Wani and S. Husain, Latest Fabrication Approaches for Surface Modified Carbon Materials: Carbon Nanotubes and Graphene, *Surface Modified Carbon Nanotubes Volume 1: Fundamentals, Synthesis and Recent Trends*, 2022, pp. 27–47, DOI: 10.1021/bk-2022-1424.ch002.

22 W. Li, S. Zhang, Q. Chen and Q. Zhong, Tailorable boron-doped carbon nanotubes as high-efficiency counter electrodes for quantum dot sensitized solar cells, *Catal. Sci. Technol.*, 2021, **11**, 2745–2752, DOI: 10.1039/d0cy02266g.

23 M. Que, W. Guo, X. Zhang, X. Li, Q. Hua, L. Dong and C. Pan, Flexible quantum dot-sensitized solar cells employing CoS nanorod arrays/graphite paper as effective counter electrodes, *J. Mater. Chem. A*, 2014, **2**, 13661, DOI: 10.1039/C4TA02052A.

24 C. V. V. M. Gopi, S. Ravi, S. S. Rao, A. E. Reddy and H.-J. Kim, Carbon nanotube/metal-sulfide composite flexible electrodes for high-performance quantum dot-sensitized solar cells and supercapacitors, *Sci. Rep.*, 2017, **7**, 46519, DOI: 10.1038/srep46519.

25 I. J. Peter, S. Vijaya, S. Anandan and P. Nithiananthi, Sb2S3 entrenched MWCNT composite as a low-cost Pt-free counter electrode for dye-sensitized solar cell and a viewpoint for a photo-powered energy system, *Electrochim. Acta*, 2021, **390**, 138864, DOI: 10.1016/j.electacta.2021.138864.

26 M. Seol, D. H. Youn, J. Y. Kim, J. Jang, M. Choi, J. S. Lee and K. Yong, Mo-Compound/CNT-Graphene Composites as Efficient Catalytic Electrodes for Quantum-Dot-Sensitized Solar Cells, *Adv. Energy Mater.*, 2014, **4**(4), 1300775, DOI: 10.1002/aenm.201300775.

27 C. V. V. M. Gopi, S. Singh, A. E. Reddy and H.-J. Kim, CNT@rGO@MoCuSe Composite as an Efficient Counter Electrode for Quantum Dot-Sensitized Solar Cells, *ACS Appl. Mater. Interfaces*, 2018, **10**, 10036–10042, DOI: 10.1021/acsami.7b18526.

28 H. T. Tung, H. P. Dang, H. K. Dan, N. T. M. Hanh, L. V. Hieu and B. V. Thang, Highly catalytic reduced graphene oxide decorated Cu2S counter electrode boosting quantum dot-sensitized solar cell performance, *Phys. Scr.*, 2024, **99**(2), 025992, DOI: 10.1088/1402-4896/ad1e49.

29 N. T. My Hanh, H. T. Tung, N. T. K. Duyen, V. C. Nguyen, L. Van Hieu, N. T. Nguyen and H. P. Dang, Effect of hydrothermal time on catalyst activity of counter electrode Cu2S-rGO composite to enhance the efficiency of quantum dot solar cells, *Ceram. Int.*, 2024, **50**, 27127–27138, DOI: 10.1016/j.ceramint.2024.05.010.

30 N. T. My Hanh, H. T. Tung, N. T. K. Duyen, V. C. Nguyen, L. Van Hieu, N. T. Nguyen and H. P. Dang, Effect of hydrothermal time on catalyst activity of counter electrode Cu2S-rGO composite to enhance the efficiency of quantum dot solar cells, *Ceram. Int.*, 2024, **50**(15), 27127–27138, DOI: 10.1016/j.ceramint.2024.05.010.

31 R. S. Lankone, J. Wang, J. F. Ranville and D. H. Fairbrother, Photodegradation of polymer-CNT nanocomposites: effect of CNT loading and CNT release characteristics, *Environ. Sci.:Nano*, 2017, **4**, 967–982, DOI: 10.1039/C6EN00669H.

32 M. S. Vidhya, G. Ravi, R. Yuvakkumar, P. Kumar, D. Velauthapillai, B. Saravanakumar and E. S. Babu, Cu2S electrochemical energy storage applications, *AIP Conf. Proc.*, 2020, **2270**, 100011, DOI: 10.1063/5.0019377.

33 M. Mirzaei and M. Bagher Gholivand, Synthesis of ruthenium sulfide nanoparticles decorated on reduced graphene oxide/multi-walled carbon nanotubes as a catalytic counter electrode for dye-sensitized solar cells exceeding 13% efficiency, *Sol. Energy*, 2022, **242**, 212–224, DOI: 10.1016/j.solener.2022.07.010.

34 Y. Bleu, F. Bourquard, V. Barnier, Y. Lefkir, S. Reynaud, A.-S. Loir, F. Garrelie and C. Donnet, Boron-doped graphene synthesis by pulsed laser co-deposition of carbon and boron, *Appl. Surf. Sci.*, 2020, **513**, 145843, DOI: 10.1016/j.apsusc.2020.145843.

35 N. Murugesan, S. Suresh, M. Kandasamy, S. Murugesan, N. Pugazhenthiran, V. P. Venkatesh, B. K. Balachandar, S. K. Kumar and M. N. M. Ansari, Facile dip-coating

assisted preparation of reduced graphene oxide-copper oxide nanocomposite thin films on aluminum substrate for solar selective absorber, *Phys. B*, 2023, **669**, 415288, DOI: **10.1016/j.physb.2023.415288**.

36 Q. Wu, R. Gao, Q. Wang, C. Yuan, C. Lin, Q. Yang, H. Tang, J. Yao, X. Zuo and G. Li, High-efficiency dye-sensitized solar cell based on carbon nanotubes-modified molybdenum nitride nanoparticles counter electrode, *Sol. Energy*, 2025, **291**, 113394, DOI: **10.1016/j.solener.2025.113394**.

37 Y. Hu, K. Cao, L. Ci and B. Mizaikoff, Selective Chemical Enhancement via Graphene Oxide in Infrared Attenuated Total Reflection Spectroscopy, *J. Phys. Chem. C*, 2019, **123**, 25286–25293, DOI: **10.1021/acs.jpcc.9b04597**.

38 F. T. Johra and W.-G. Jung, Hydrothermally reduced graphene oxide as a supercapacitor, *Appl. Surf. Sci.*, 2015, **357**, 1911–1914, DOI: **10.1016/j.apsusc.2015.09.128**.

39 J. Chen, E. Wang, J. Mu, B. Ai, T. Zhang, W. Ge and L. Zhang, CNTs–C@TiO2 composites with 3D networks as anode material for lithium/sodium ion batteries, *J. Mater. Sci.*, 2019, **54**, 592–604, DOI: **10.1007/s10853-018-2814-2**.

40 X. Zhang, L. Duan, X. Zhang, X. Li and W. Lü, Preparation of Cu2S@rGO hybrid composites as anode materials for enhanced electrochemical properties of lithium ion battery, *J. Alloys Compd.*, 2020, **816**, 152539, DOI: **10.1016/j.jallcom.2019.152539**.

41 I. Mínguez-Bacho, M. Courté, C. Shi and D. Fichou, Controlling the nanomorphology of thin conformal Cu2S overlayers grown on Cu2O compact layers and nanowires, *Mater. Lett.*, 2015, **159**, 47–50, DOI: **10.1016/j.matlet.2015.06.064**.

42 L. Torrisi, L. Silipigni, G. Salvato, M. Cutroneo and A. Torrisi, Graphene-based materials: properties, advancements and applications, *Radiat. Eff. Defects Solids*, 2022, **177**, 1151–1165, DOI: **10.1080/10420150.2022.2136075**.

43 Y. Zhang, Y. Ji, Z. Wang, S. Liu and T. Zhang, Electrodeposition synthesis of reduced graphene oxide–carbon nanotube hybrids on indium tin oxide electrode for simultaneous electrochemical detection of ascorbic acid, dopamine and uric acid, *RSC Adv.*, 2015, **5**, 106307–106314, DOI: **10.1039/C5RA24727F**.

44 W. Li, G. Long, Q. Chen and Q. Zhong, High-efficiency layered sulfur-doped reduced graphene oxide and carbon nanotube composite counter electrode for quantum dot sensitized solar cells, *J. Power Sources*, 2019, **430**, 95–103, DOI: **10.1016/j.jpowsour.2019.05.020**.

45 O. López-Rojas, M. del Socorro Aguilar, J. de Jesús Ku-Herrera, R. M. Jiménez-Barrera, V. H. López, J. García, E. Reyes-Francis, I. Zarazúa, T. López-Luke, O. López-Rojas, *et al.*, Photoelectrochemical Study of the Performance Enhancement of CNT-Based Counter Electrodes by Adding N-S Doped rGO in QD Solar Cells, *J. Electron. Mater.*, 2025, **54**, 1141–1156, DOI: **10.1007/s11664-024-11606-8**.

46 V. Chakrapani, D. Baker and P. V. Kamat, Understanding the Role of the Sulfide Redox Couple (S^{2-}/S_n^{2-}) in Quantum Dot-Sensitized Solar Cells, *J. Am. Chem. Soc.*, 2011, **133**, 9607–9615, DOI: **10.1021/ja203131b**.

47 P. V. Kamat, Quantum Dot Solar Cells. Semiconductor Nanocrystals as Light Harvesters, *J. Phys. Chem. C*, 2008, **112**, 18737–18753, DOI: **10.1021/jp806791s**.

48 C. V. V. M. Gopi, S. Singh, A. E. Reddy and H. J. Kim, CNT@rGO@MoCuSe Composite as an Efficient Counter Electrode for Quantum Dot-Sensitized Solar Cells, *ACS Appl. Mater. Interfaces*, 2018, **10**, 10036–10042, DOI: **10.1021/acsami.7b18526**.

49 C. V. V. M. Gopi, S. Ravi, S. S. Rao, A. E. Reddy and H. J. Kim, Carbon nanotube/metal-sulfide composite flexible electrodes for high-performance quantum dot-sensitized solar cells and supercapacitors, *Sci. Rep.*, 2017, **7**, 46519, DOI: **10.1038/srep46519**.

50 J. Zeng, W. Wang, Y. Lin, Z. Zhang, Z. Li, H. Rao, Z. Pan and X. Zhong, Nitrogen-doped mesoporous carbon combined with carbon nanotubes as counter electrode catalysts for quantum dot sensitized solar cells with record efficiency, *Sol. Energy*, 2024, **276**, 112699, DOI: **10.1016/j.solener.2024.112699**.